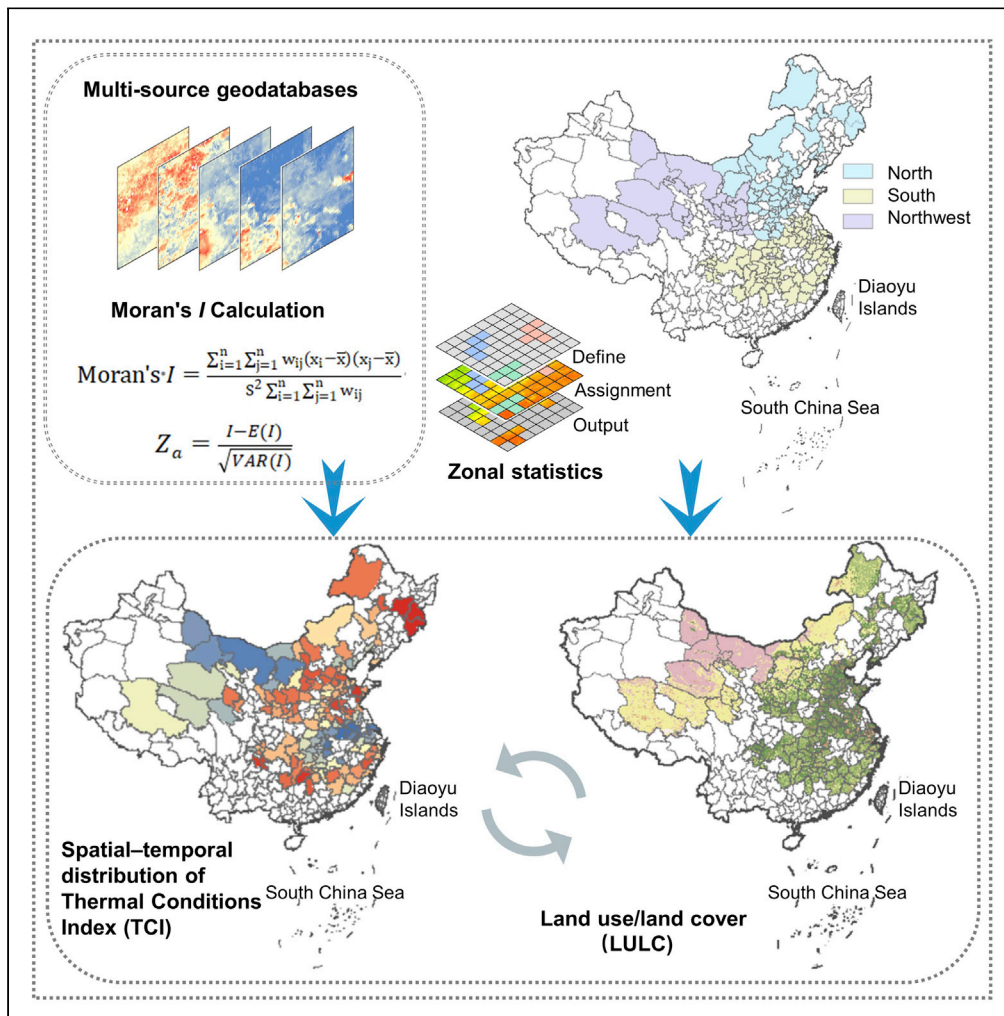# iScience

Article

Regional thermal environment changes: Integration of satellite data and land use/land cover

Jiayi Ren, Jun Yang, Feng Wu, Wei Sun, Xiangming Xiao, Jianhong (Cecilia) Xia

yangjun8@mail.neu.edu.cn (J.Y.)
wufeng@igsnrr.ac.cn (F.W.)
wsun@niglas.ac.cn (W.S.)

Highlights

Explored distribution of region thermal environment based on geostationary satellite data

TCI in Northwest China decreased from 2017 to 2021, whereas in North and South increased

Average TCI of forest is the highest and bare land is the lowest

The TCI for artificial surfaces are North (0.633) > Northwest (0.554) > South (0.384)

Article

Regional thermal environment changes: Integration of satellite data and land use/land cover

Jiayi Ren,[1] Jun Yang,[1,2,3,8,*] Feng Wu,[4,*] Wei Sun,[5,*] Xiangming Xiao,[6] and Jianhong (Cecilia) Xia[7]

SUMMARY

Land surface temperature (LST) is subject to location and environmental influences, which makes quantification difficult in terms of timeliness. Based on 10-d geostationary satellite LST TCI products, we quantitatively evaluated the thermal environment differentiation of various ground objects in North, South, and Northwest China from 2017 to 2021. We found that the thermal condition index (TCI) in Northwest China decreased, whereas it increased in North and South China. In contrast, Moran's _I_ index increased in Northwest and South China, with strong spatial agglomeration. The TCI for artificial surfaces decreased from North (0.633) to Northwest (0.554) and South China (0.384). The bare land TCI was always the lowest among the land use/land cover (LULC) types in each region. Our results reflect the LULC thermal environment of China against the background of new urbanization and provide theoretical support for scientific planning to improve the ecological environment.

INTRODUCTION

Sharing responsibility for reducing carbon dioxide emissions to limit global warming to 1.5°C became a point of contention among countries at the Working Group III meeting of the Sixth Assessment Report of the IPCC.[1,2] Carbon emissions from agriculture, forestry, and land use are highly uncertain,[1] mainly because of changes in land use/land cover (LULC) caused by human activities, such as deforestation, urbanization, and fragmentation of arable land.[3,4] The statistical analysis of greenhouse gas emissions and human activities in global natural systems by Yue et al.[5] indicates that human emissions exert additional pressure on regional climates and the urban thermal environment, resulting in urban heat islands (UHI) and other problems. Luo et al.[6] showed that summer heat stress in major urban agglomerations in China has been significantly aggravated. At present, the development of China's urbanization has changed from the traditional pursuit of rapid growth to a focus on quality improvement.[7,8] Improvements in the urban thermal environment attract much attention, but regional differences in related achievements persist.[9,10]

Land surface temperature (LST) can reflect the degree of surface warming and is typically used as a parameter to monitor the thermal environment.[11,12] With the advent of remote sensing technology, global and long time-series image observation data can be obtained based on satellite platforms. Considerable achievements have been made in inversion methods, spatiotemporal distribution, simulation, and prediction.[13–15] Zhou et al.[16] and Xiang et al.[17] reported that farmland could reduce LST by 0.6°C at night. However, most LST products are provided by polar–orbiting satellites, which perform only one or two observations per day in the same area, and their flyby times are fixed. The lack of comprehensive surface temperature records at all times of the day leads to a lack of comparability between products; in addition, studies are usually limited to day and night or specific times.

This gap can be filled by incorporating LST observations from geostationary satellites.[18,19] The Copernicus Global Land Service provides global 5-km/h LST data based on a series of geostationary satellites (Meteosat, GOES, MTSAT/Himawari), covering most of the Earth's land surface between latitudes of 60° S to 70° N, including hourly LST, 10–day LST daily cycle, and 10–day LST thermal condition index (TCI) products.[20] These products are more advantageous for studying spatiotemporal variations in the large-scale thermal environment. In addition, vegetation health indices have been derived from the TCI.[21] TCI data calculated based on the 10–day LST daily cycle represents the thermal degree of any given land pixel relative to its maximum temperature range and can well reflect the environmental information under the state of the surface energy balance, with a range between 0 and 1[21,22]. Therefore, this study selected TCI composite data

[1]School of Humanities and Law, Northeastern University, Shenyang 116029, China

[2]Human Settlements Research Center, Liaoning Normal University, Dalian 116029, China

[3]Jangho Architecture College, Northeastern University, Shenyang 110169, China

[4]Key Laboratory of Regional Sustainable Development Modeling, Institute of Geographic Sciences and Natural Resources Research, CAS, Beijing 100101, China

[5]Nanjing Institute of Geography and Limnology, Key Laboratory of Watershed Geographic Sciences, Chinese Academy of Sciences, Nanjing 210008, China

[6]Department of Microbiology and Plant Biology, Center for Earth Observation and Modeling, University of Oklahoma, Norman, OK 73019, USA

[7]School of Earth and Planetary Sciences (EPS), Curtin University, Perth, WA 65630, Australia

[8]Lead contact

*Correspondence:
yangjun8@mail.neu.edu.cn (J.Y.),
wufeng@igsnrr.ac.cn (F.W.),
wsun@niglas.ac.cn (W.S.)
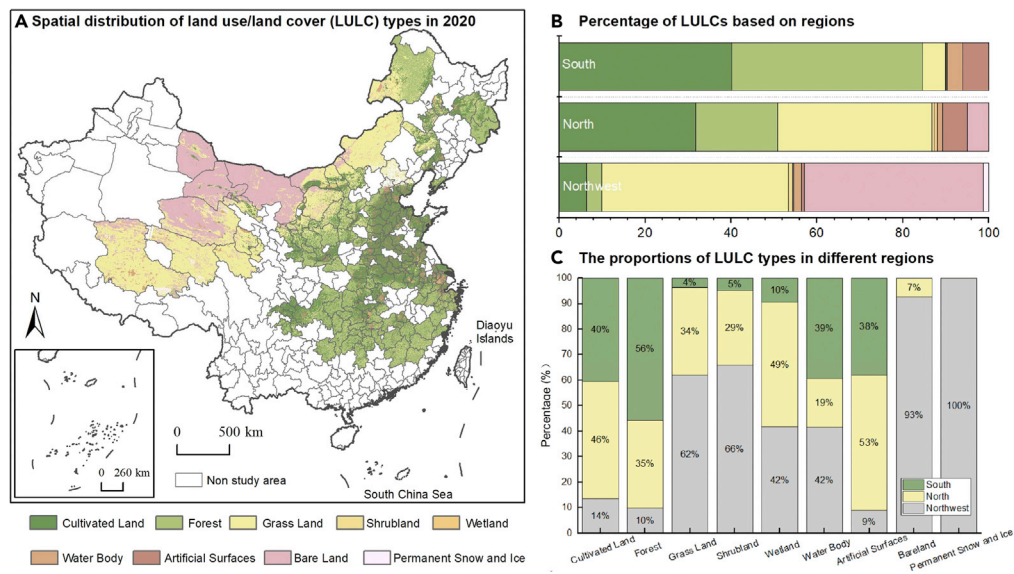
https://doi.org/10.1016/j.isci.2022.105820

Figure 1. Spatial distribution of land use/land cover (LULC) types in North, Northwest and South China

(A) Spatial distribution of land use/land cover (LULC) types in different regions.

(B) Percentage of land use/land cover (LULC) in different regions.

(C) Proportions of land use/land cover (LULC) types in different regions.

generated from August 1 to 11 of each year from 2017 to 2021. Such timeliness data can comprehensively reflect the characteristics of the thermal environment.

To date, the UHI effect has widely been studied in many cities worldwide, but its causes differ.[22–24] In most cities, the UHI effect is more obvious in summer than in winter.[25–27] Studies on the driving factors have mainly focused on LULC, landscape patterns, human activities, meteorological conditions, and geographical location.[28–30] In terms of LULC, studies have found that green land and water can alleviate the UHI effect, whereas bare soil can increase LST.[31–33] The degree of fragmentation of ground object patches and the degree of distribution dispersion have different effects on LST in a region and its surrounding areas.[34,35] The urban agglomeration effect should be considered in thermal environment research, as air pollution and the urban climate have cross–regional mobility.[36] It is thus necessary to explore LULC and thermal environment response patterns on a large scale.[37] The current classification of key landscapes affecting the thermal environment and considering regional effects is relatively vague, and other land types comprising vegetation (e.g., cultivated land, forest, or grass) are seldom considered.

Studies have shown that China (73°33′–135°05′ E, 3°51′–53°33′ N) is one of the countries experiencing most extreme heat conditions, and decreasing trends have been found in the frequency of cool days.[38] Luo et al.[39] found that large contiguous heatwaves in China showed different characteristics in different geographical locations. Moreover, the temperature difference was considerably large between North and South China in winter, whereas it was relatively small in summer. To avoid the excessive influence of solar radiation, we selected summer as the study period. In addition, with the continuous strengthening of the social economy, China's urbanization is shifting from a stage of rapid development to a stage of deepening development, so that the population will inhabit cities having a good developmental foundation and strong carrying capacities, likely leading to the emersion of new cities.[10,40] Considering data validity, we selected 55 cities in North China, 74 cities in South China, and 24 cities in Northwest China to measure spatial–temporal changes in the thermal environment in the past five years and quantitatively analyze differentiation rules for the LULC thermal environment.

RESULTS

Land utilization type

The LULC data were visualized based on the vector boundary of the study area, and the spatial distribution of each region in China was obtained (Figure 1A). Overall, vegetation (cultivated land, forest, and
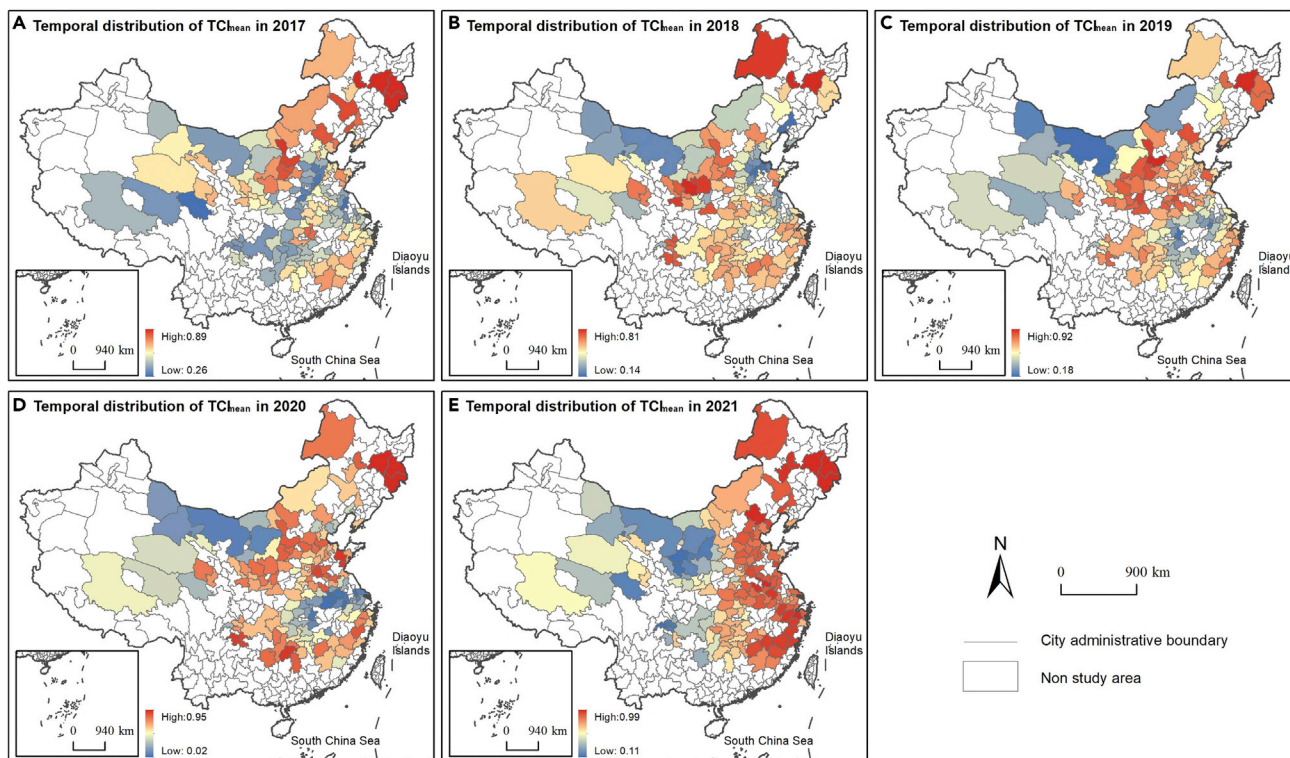
Figure 2. Spatial and temporal distribution of TCI$_{mean}$ in different years

grassland) covered the largest area. Forests in South China accounted for 44%, followed by cultivated land, which accounted for 40%. In North China, 46% of the land was grassland and 32% was forest, whereas the LULC types in Northwest China were grassland and bare land, accounting for 43 and 42%, respectively. Furthermore, on a large scale, the area covered by artificial surfaces was relatively low, accounting for only 6% in both North and South China, and only 1% in Northwest China (Figure 1B). Industrial cities in North China have a long history, with 53% of the land comprising artificial surfaces (Figure 1C), with 38% of the artificial surfaces located in South China in a concentrated spatial distribution. Wetlands and water bodies were usually located close to the vegetation. Shrublands were mostly found in cities, whereas permanent snow and ice were only found in Northwest China (only 1%).

Temporal and spatial characteristics of the thermal environment
Spatial–temporal distribution

Based on the urban boundaries of the study area, the TCI data were statistically divided into different areas, and the statistical method employed was considering the average (TCI$_{mean}$). As shown in Figure 2, the TCI showed significant spatial and temporal heterogeneity from 2017 to 2021. Spatially, the TCI was lower in most cities in North and Northwest China, and relatively higher in South China, whereas this feature changed over time. Figures 3A–3C shows TCI$_{mean}$ threshold and average values. The averages of the national TCI$_{mean}$ in 2017, 2018, 2019, 2020, and 2021 were 0.535, 0.524, 0.593, 0.569, and 0.695, respectively. In terms of the average (Figure 3C), TCI$_{mean}$ in Northwest China showed a decreasing trend from 0.537 in 2017 to 0.396 in 2021. Notably, TCI$_{mean}$ in North China increased from 0.576 in 2017 to 0.773 in 2021, especially in Northeast China and Beijing-Tianjin-Hebei urban agglomeration. By 2021, TCI$_{mean}$ was overall higher in the eastern region. In South China, TCI$_{mean}$ decreased to 0.494 in 2020, but increased significantly to 0.734 by 2021.

Figure 4 shows the percentage stack diagram of TCI$_{mean}$ values for cities. For cities in South China (Figure 4A), the TCI$_{mean}$ values mostly remained stable from 2017 to 2020, whereas the urban agglomeration in the middle and lower reaches of the Yangtze River significantly decreased in 2020. In 2021, TCI$_{mean}$ increased significantly, with most cities (47/74) reaching values above 0.7; the highest values were 0.984
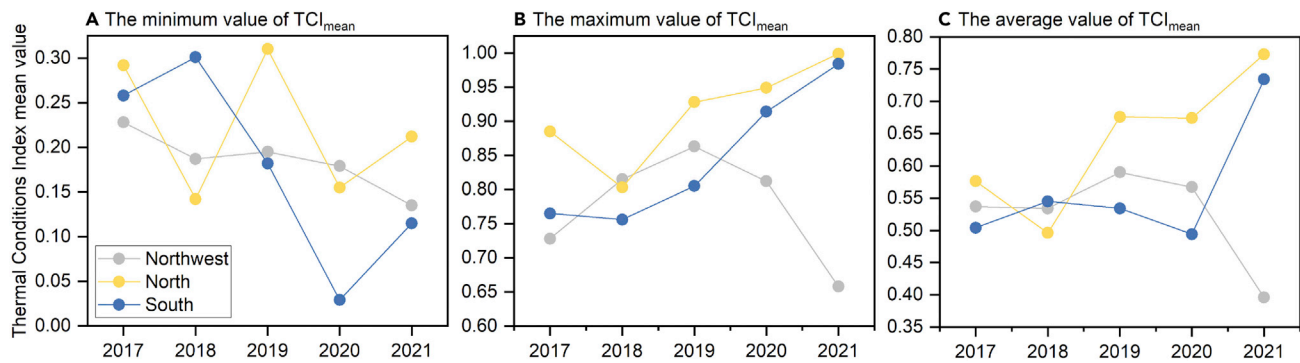
Figure 3. TCI_mean zoning statistics based on the cities

TCI_mean: Mean values of the thermal condition index obtained by partition statistics.

(Suzhou), 0.978 (Shaoxing), and 0.962 (Bozhou). The TCI_{mean} values of cities in North China (Figure 4B) differed greatly and were generally low in 2017 and 2018, then substantially increased in 2019, and decreased again in 2020. On the contrary, TCI_{mean} in cities in Northwest China (Figure 4C) was generally higher in 2017 and lower in 2021.

Spatial autocorrelation analysis

The global Moran index was calculated using the ArcGIS 10.7 spatial statistical tool. In this study, two definitions of spatial relations of specified elements were selected: Inverse–Distance (Figure 5A) and Contiguity–Edges–Corners (Figure 5B). Inverse–Distance indicates that compared with distant factors, adjacent factors have a greater influence on the target factors. Contiguity–Edges–Corners indicates that the shared boundary, node, or overlapping surface elements affect the calculation of the target surface elements. The results showed that in most cases, the p-value was less than 0.01, and the Z score was greater than 2.58, indicating that TCI_{mean} was not randomly distributed, with 99% confidence. The overall performance of Moran's I index in Northwest and South China increased, among which Northwest China showed an obvious spatial agglomeration in 2019, and Moran's I index was above 0.5 (Inverse–Distance was 0.531 and Contiguity–Edges–Corners was 0.594). In South China, Moran's I index was relatively high, with a strong spatial agglomeration, reaching its highest value in 2020 (Inverse-Distance) and 2021 (Contiguity–Edges–Corners), with values of 0.691 and 0.628, respectively. For North China, Moran's I calculated in the Inverse-Distance mode was lower than that in the Contiguity–Edges–Corners mode, but both showed an increasing trend after decreasing to the lowest value (0.267) in 2019, with values of 0.638 and 0.527 in 2017 and 2021, respectively (Contiguity–Edges–Corners).

Local spatial autocorrelation analysis showed the relationship between the thermal environment in a certain area and neighboring areas, as shown in Figure 6. There were many spatially independent cities in Northwest China. The cities in North China were mainly of the High–High aggregation type, and the Beijing–Tianjin–Hebei region was of the High–Low aggregation type between 2018 and 2020 (Figures 6B–6D), which is consistent with the spatial distribution shown in Figure 4. The overall urban thermal environment in South China was more concentrated in space. Here, cities in the middle and lower reaches of the Yangtze River showed Low–Low clustering patterns in 2019 and 2020 (Figures 6C and 6D) and High–High clustering patterns in 2017 (Figure 6A) and 2021 (Figure 6E). Due to the small number of selected cities and the large urban spacing, the spatial agglomeration of the TCI in Northwest China was not significant.

Response model of the thermal environment and LULC

Based on the LULC raster, the TCI data were partitioned for statistics, and TCI_{mean} values for each ground object type were obtained, as shown in Table 1. The TCI value represents the thermal degree at the pixel level relative to its maximum temperature range, which can reflect the health status of the vegetation to a certain extent.[41] Overall, the average TCI of forests in Northwest and North China was the highest, at 0.745 and 0.776, respectively. Other vegetation types also showed spatial differences (for example, the TCI of grassland was 0.471 in Northwest China but 0.634 in South China, whereas shrubland reached values of 0.740 in South China but 0.546 in North China). The TCI of artificial surfaces decreased from North
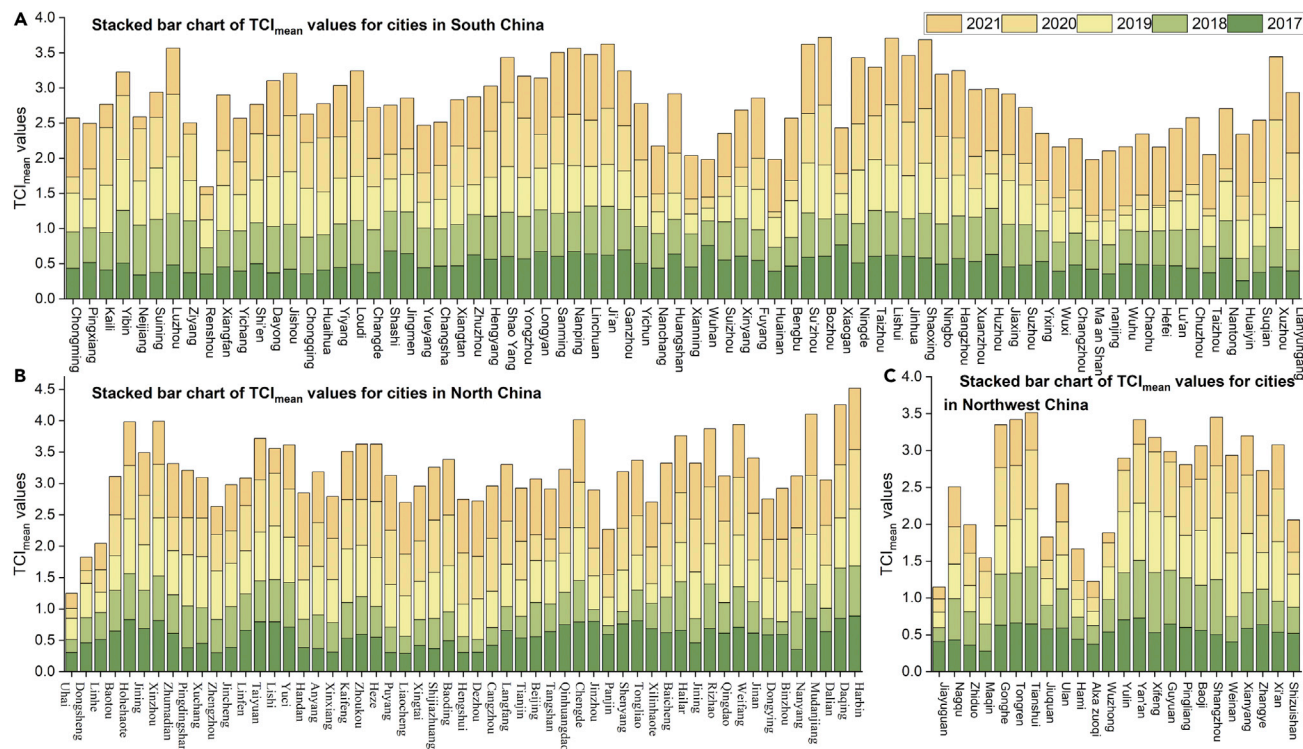
Figure 4. Stacked bar chart of TCI$_{mean}$ values for every city from 2017 to 2021
(A) Stacked bar chart of TCI$_{mean}$ values for cities in South China.
(B) Stacked bar chart of TCI$_{mean}$ values for cities in North China.
(C) Stacked bar chart of TCI$_{mean}$ values for cities in Northwest China.

(0.633) to Northwest (0.554) and South China (0.384). The TCI of bare land was always the lowest among the terrain types in each region, and the TCI of water bodies in Northwest China (0.503) and North China (0.560) was higher than that in South China (0.395). Although the original raster data revealed the TCI differences of many ground object types, in some cases pixel values were missing or LULC values zero. Therefore, we created a 5×5-km grid to match the spatial resolution of synchronous satellite data according to the administrative boundaries of the research area, which was spatially linked to the LULC and TCI data. The majority method was used to determine the cell value as the most common value among all pixels in the area, and then, the assigned cell was obtained after removing null values and outliers. Finally, the number of cells in Northwest China was 75639, that in North China was 67567, and that in South China was 52232. The numerical distribution characteristics of the TCI were studied based on the grid, and the results are shown in Figure 7.

The median value has the advantage of not being affected by large or small amounts of data and is more representative of the whole dataset. The average TCI based on the grid was mostly lower than the median, except for some land features in South China, such as cultivated land (TCI$_{Mean}$ = 0.465, TCI$_{Median}$ = 0.426), shrubland (TCI$_{Mean}$ = 0.211, TCI$_{Median}$ = 0.191), water bodies (TCI$_{Mean}$ = 0.403, TCI$_{Median}$ = 0.394), and artificial surfaces (TCI$_{Mean}$ = 0.329, TCI$_{Median}$ = 0.266). The TCI value distribution of LULC in South China (Figure 7C) significantly differed from that in Northwest and North China (Figures 7A and 7B), with cultivated land, shrubland, and shrubland being the most significant. The TCI of surface objects of various vegetation types was generally higher than that of artificial surfaces and bare land. Based on Figures 1 and 2D, vegetation health played an important role in the urban thermal environment, whereas water bodies had similar but weaker effects than vegetation.

DISCUSSION

Chen et al.[42] reported that half a degree plays a crucial role in reducing and delaying global land exposure to hot extremes. The regional thermal environment is complex in space and time and profoundly affects the
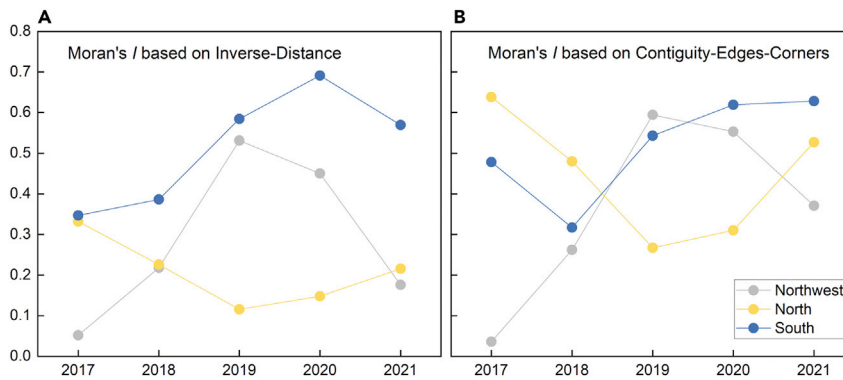
Figure 5. Distribution of Moran's *I* values
(A) Moran's *I* calculated based on Inverse–Distance.
(B) Moran's *I* calculated based on Contiguity–Edges–Corners.

comfort level of human settlements and sustainable development.[40,43] Based on 10–day LST TCI composite products provided by synchronous satellites, we used geographical information system spatial analysis and quantitative remote sensing technology to explore the spatial–temporal distribution and spatial autocorrelation of the regional thermal environment during summer in China over a period of five years. Moreover, LULC data were combined to analyze the thermal differentiation of various ground objects in different regions, reflecting the thermal environment of China's evolving land use to provide theoretical support for scientific planning to improve the ecological environment.

Selection of geostationary satellite data

Most studies retrieve LST data from polar-orbiting satellite data, but the study scale can affect the results. For example, Alavipanah et al.[44] compared LST differences between MODIS and INSAT-3D data at high temperature. Goldblatt et al.[45] reported that Landsat-5,- 7, and -8 data are suitable for studying the micro-scale LST. Yang et al.[46] used Landsat 8 data to analyze the correlation between urban wind and LST at grid scale. The grid in that study was increased from 25 × 25 m to 150 × 150 m with a step size of 25 m, and the authors found that the larger the scale, the weaker the correlation. However, the LST changes with time, and remote sensing data obtained by polar-orbiting satellites have a low temporal resolution, which is not conducive to reflect the urban thermal environment under normal circumstances.

In addition, existing thermal environment assessment procedures are limited to simple (mainly two–parameter) index construction in areas such as public meteorological services, preventive planning, urban design, and climate change.[47,48] Some studies reflect the urban thermal environment quality by simulating outdoor thermal comfort.[49,50] ISB Commission 6 has built the universal thermal climate index (UTCI) based on the most advanced multi–node temperature regulation model, which is an important step forward in incorporating air temperature, wind, and humidity while considering of the urban thermal environment and living comfort.[48]

We performed comprehensive investigations to understand differences in the thermal environment of various LULC types from a large–scale perspective. We thus selected TCI data calculated via 10-day LST daily cycle products provided by geostationary satellites. The product is suitable for applications that do not require attention to daily changes in LST over a short period, or where LST daily cycles do not require gaps arising because of cloud cover and have outliers removed.[51,52] Because data averages are sensitive to outliers, this product provides the median LST rather than the average LST, providing a better representation of the state of the thermal environment during the study period.

Spatial autocorrelation of the urban thermal environment

Guo et al.[53] studied the thermal environment based on community level and reported that the global autocorrelation Moran's *I* value of LST exceeded 0.7, with a strong positive spatial correlation. In this study, the spatial and temporal distribution of the TCI was obtained using the zoning statistical method. Figure 4 shows the distribution of TCI_mean for all cities classified by region. Overall, TCI_mean values in Northwest
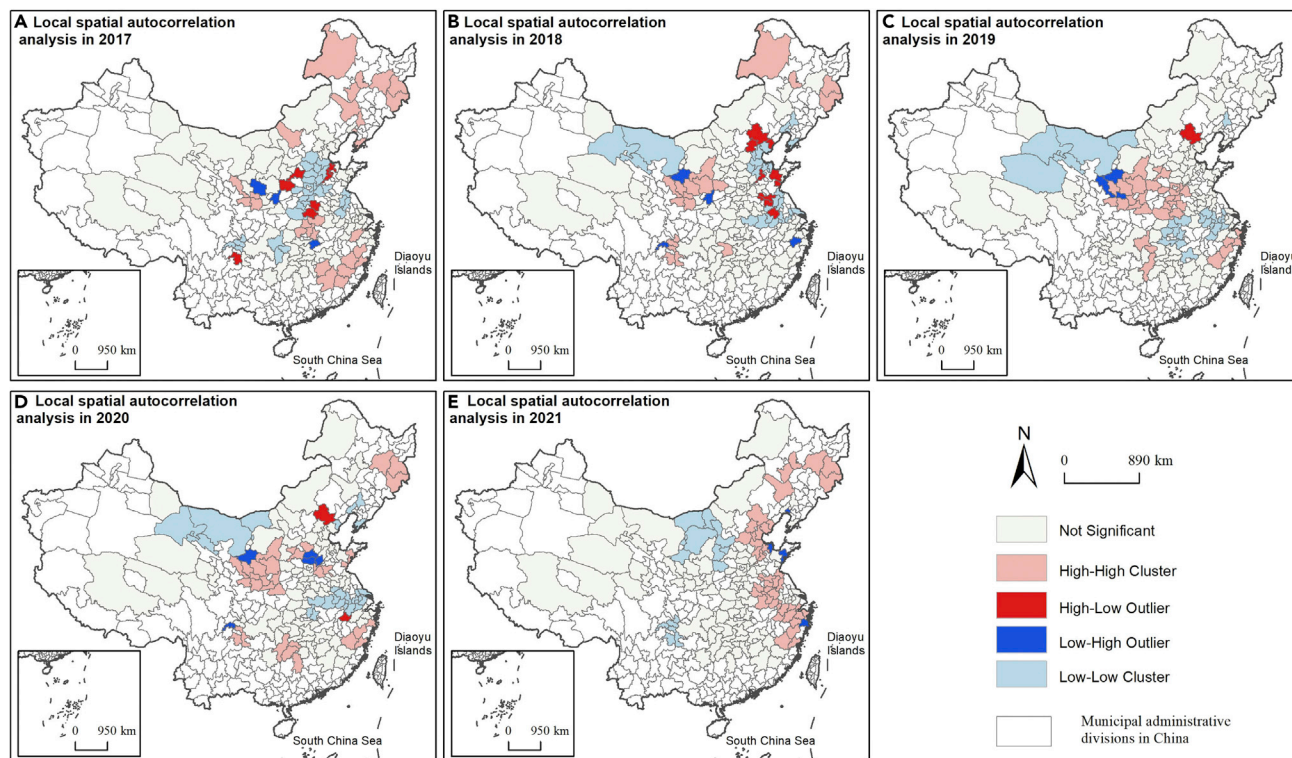
Figure 6. Results of local autocorrelation analysis of TCI$_{mean}$ from 2017 to 2021
(A) Local autocorrelation in 2017.
(B) Local autocorrelation in 2018.
(C) Local autocorrelation in 2019.
(D) Local autocorrelation in 2020.
(E) Local autocorrelation in 2021.

China were lower than those in Eastern China, but they changed dynamically. The TCI$_{mean}$ values of some cities in Northwest China were higher in 2017 (e.g., Jiayuguan, Jiuquan, Wuzhong) and lower in 2021 (e.g., Jiayuguan, Yulin, Yan'an and Xifeng). Figures 5 and 6 show that the TCI had a certain spatial correlation, with Z = 1.155, p = 0.248 (Inverse–Distance), and p = 0.559 (Contiguity–Edges–Corners) in 2017 and Z = 2.240 and p = 0.025 (Contiguity–Edges–Corners) in 2018 for Northwest China. The spatial correlation of these data could not be explained.

Table 1. Partition statistics for TCI based on LULC

|	Northwest		North		South	
	Mean	STD	Mean	STD	Mean	STD
Cultivated Land	0.676	0.281	0.699	0.267	0.501	0.336
Forest	0.745	0.214	0.776	0.227	0.668	0.312
Grass Land	0.471	0.314	0.585	0.266	0.634	0.327
Shrubland	0.553	0.326	0.546	0.243	0.740	0.294
Wetland	0.390	0.304	0.656	0.243	0.437	0.290
Water Body	0.503	0.315	0.560	0.265	0.395	0.286
Artificial Surfaces	0.554	0.290	0.633	0.293	0.384	0.334
Bare land	0.273	0.212	0.345	0.209	0.347	0.205
Permanent Snow and Ice	0.540	0.338	–	–	–	–
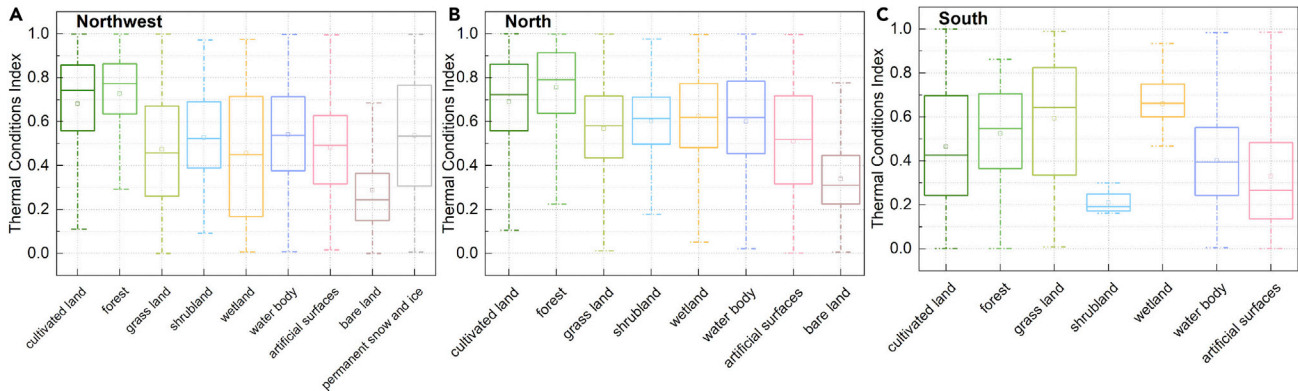
Figure 7. Grid-based land use land cover (LULC) and TCI numerical distribution boxline plot

(Boxes represent 25–75% values, whisker lines represent interquartile range as IQR, horizontal lines represent median values, and rectangles represent mean values).

(A) Numerical distribution of LULC and TCI in Northwest China.

(B) Numerical distribution of LULC and TCI in North China.

(C) Numerical distribution of LULC and TCI in South China.

Differentiation of the LULC thermal environment

The rapid transformation of urban land significantly affects the characteristics of the ecosystem and thermal environment, and previous studies showed that the most important factors leading to differences in UHI were the transformation of man–made land cover and natural land cover, landscape configuration, and anthropogenic heat release.[54,55] Urban high-temperature areas are related to impervious water surfaces, whereas minimum temperatures are related to vegetation cover and water bodies.[56–58] Feng et al.[59] discussed the influence of landscape composition, morphology, and space layout and the internal LST on environmental temperature and cooling rate. They found that the more complex the patch shape (vegetation and water bodies) and the more scattered the layout, the lower the internal temperature, the greater the impact on the surrounding area, and the greater the cooling rate. Based on these previous results, we first discussed the spatial distribution pattern of LULC, and then conducted zoning statistics on this distribution and the TCI on the city and grid levels. We found that the LULC TCI differed at different scales. At the regional scale, the TCI difference between forest (highest value) and bare land (lowest value) was 0.472 in Northwest China, whereas that difference was 0.431 in North China. The TCI difference between the shrubland (highest value) and bare land (lowest value) in South China was 0.393.
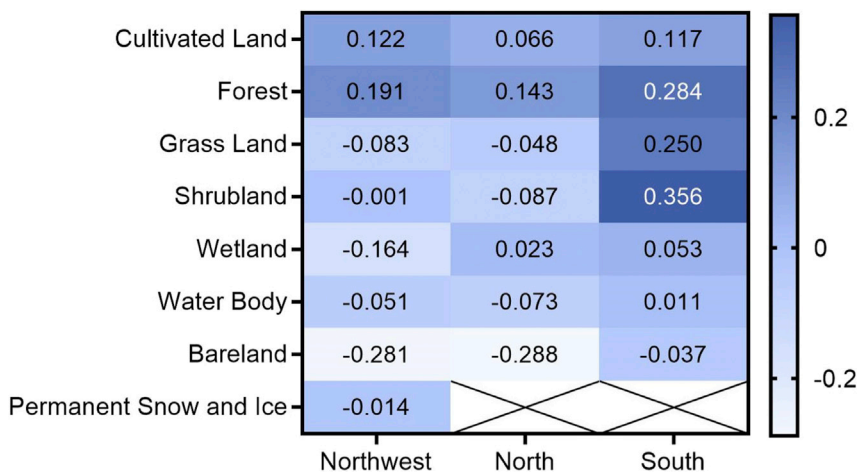

Figure 8. Difference between TCI_LULC and TCI_Artificial Surfaces values

With the expansion of central urban areas and the agglomeration of towns, impervious surface areas have replaced natural surfaces. Tran et al.[60] demonstrated the warming effect of urban sprawl, and showed that a 1% increase in urban areas will increase the LST by 0.075°C–0.108°C. In addition, more than 81% of impervious surfaces have been labeled as heat sources, whereas vegetation and water function as heat sinks.[61] Figure 8 shows the TCI differences between various ground objects and artificial surfaces. The values for cultivated land and forest were generally higher. Grassland and shrubland in Southern China showed the highest values for artificial surfaces. The cooling effect of water bodies is related to their spatial form, connectivity, and area.[62,63] Our results indicated that there was little difference between the TCI of water bodies and artificial surfaces, which was related to the low aggregation degree and small area of urban water bodies at a large scale.

In recent years, China has made remarkable achievements in afforestation programs, such as the "Three-North Shelterbel," "Return of farmland to forest," and "Control of sand sources in Beijing and Tianjin" projects. Surveys have shown that artificial afforestation has long been the largest in the world. From 2000 to 2018, China's forest area increased by 45 million km,[2] an increase of 26.90%.[64] China's new urbanization focus has not only effectively reduced pollution emissions and improved energy efficiency but has also entailed great ecological effects.[65,66] The results of this study showed that the TCI of vegetation was usually higher than that of impervious water surfaces and bare land, and the spatiotemporal heterogeneity of the TCI was closely related to LULC. From a macro point of view, TCI_{mean} has been increasing in most Chinese cities in the last five years, especially in Northeast China, implying that the urban thermal environment has improved. Simultaneously, urbanization is necessary to promote social progress, and the Chinese government regards sustainable urbanization as an engine of modernization and economic growth.[67,68] Therefore, a new urbanization mode should actively be explored for LULC based on the comfort of living, namely intensive, efficient, urban–rural integration, harmonious, and sustainable urbanization.

Limitations of the study

We could not calculate the TCI value based on the selected synchronous satellite data when the effective LST value was extremely small; therefore, some pixel values were missing. In the future, these missing pixels can be filled using polar-orbiting satellite data (e.g., Landsat 8 and MODIS) from similar periods, as they are suitable for small-scale studies.[44,45] The median 10–day maximum LST values used in the TCI calculations corresponded to the time range between local noon and 1 h and local noon +2 h during synthesis, because the maximum LST values tend to occur after noon, and the local noon is determined by the time the zenith angle of the Sun reaches its minimum for a particular day. The presence of an unavailable LST data during such a time frame implies a missing TCI value, and the LULC data of this study were from 2020. Based on these data, the differentiation for LULC and TCI was studied. The seasonal or interannual characteristics of this differentiation should be studied further in the future.

STAR★METHODS

Detailed methods are provided in the online version of this paper and include the following:

- KEY RESOURCES TABLE
- RESOURCE AVAILABILITY
  - Lead contact
  - Materials availability
  - Data and code availability
- METHOD DETAILS
  - Data
  - Moran's *I* calculation
  - Statistical analysis

DECLARATION OF INTERESTS

This manuscript has not been published or presented elsewhere in part or in entirety and is not under consideration by another journal. We have read and understood your journal's policies, and we believe that neither the manuscript nor the study violates any of these. The authors declare no competing interests.

INCLUSION AND DIVERSITY

We support inclusive, diverse, and equitable conduct of research.

REFERENCES

1. IPCC (2022). Climate change 2022: mitigation of climate change. https://www.ipcc.ch/report/sixth-assessment-report-working-group-3/.

2. Wang, Z.N., Yuan, J.S., Pang, B., and Huang, L. (2022). The interpretation and highlights of IPCC AR6 WGIII report climate change 2022: mitigation of climate change. Climate Change Research. https://kns.cnki.net/kcms/detail/11.5368.P.20220818.1738.002.html.

3. Derdouri, A., Wang, R., Murayama, Y., and Osaragi, T. (2021). Understanding the links between LULC changes and SUHI in cities: insights from two–decadal studies (2001–2020). Rem. Sens. 13, 3654. https://doi.org/10.3390/rs13183654.

4. Liang, L., Wang, Z., and Li, J. (2019). The effect of urbanization on environmental pollution in rapidly developing urban agglomerations. J. Clean.Prod. 237, 117649. https://doi.org/10.1016/j.jclepro.2019.117649.

5. Yue, X.L., and Gao, Q.X. (2018). Contributions of natural systems and human activity to greenhouse gas emissions. Adv Clim Change Res. 9, 243–252. https://doi.org/10.1016/j.accre.2018.12.003.

6. Luo, M., and Lau, N. (2021). Increasing human-perceived heat stress risks exacerbated by urbanization in China: a comparative study based on multiple metrics. Earth's Future 9. https://doi.org/10.1029/2020EF00184.

7. Yu, B. (2021). Ecological effects of new–type urbanization in China. Renew. Sust. Energ. Rev. 135, 110239. https://doi.org/10.1016/j.rser.2020.110239.

8. Yu, W., Yang, J., Sun, D., Yu, H., Yao, Y., Xiao, X., and Xia, J. (2022). SpatialTemporal patterns of network structure of human settlements competitiveness in resource–based urban agglomerations. Front. Environ. Sci. 10, 893876. https://doi.org/10.3389/fenvs.2022.893876.

9. Guan, X., Wei, H., Lu, S., Dai, Q., and Su, H. (2018). Assessment on the urbanization strategy in China: achievements, challenges and reflections. Habitat Int. 71, 97–109. https://doi.org/10.1016/j.habitatint.2017.11.009.

10. Yang, Z., Shao, S., Xu, L., and Yang, L. (2022). Can regional development plans promote economic growth? City–level evidence from China. Socio–Econ. Plan. Sci. 83, 101212. https://doi.org/10.1016/j.seps.2021.101212.

11. Hu, D.Y., Qiao, K., and Wang, X.L. (2015). Land surface temperature retrieval from Landsat 8 thermal infrared data using mono–window algorith. J Remote Sens 19, 964–976. https://doi.org/10.1109/TGRS.2021.3088482.

12. Svendsen, L., Keenlyside, N., Bethke, I., Gao, Y., and Omrani, N.-E. (2018). Pacific contribution to the early twentieth-century warming in the Arctic. Nature Clim. Change 8, 793–797. https://doi.org/10.1038/s41558-018-0247-1.

13. Liu, X., Zhou, Y., Yue, W., Li, X., Liu, Y., and Lu, D. (2020). Spatiotemporal patterns of summer urban heat island in Beijing, China using an improved land surface temperature. J. Clean.Prod. 257, 120529. https://doi.org/10.1016/j.jclepro.2020.120529.

14. Pepin, N., Deng, H., Zhang, H., Zhang, F., Kang, S., and Yao, T. (2019). An examination of temperature trends at high elevations across the Tibetan Plateau: the use of MODIS LST to understand patterns of elevation–dependent warming. J. Geophys. Res. Atmos. 124, 5738–5756. https://doi.org/10.1029/2018jd029798.

15. Wang, D., Chen, Y., Hu, L., Voogt, J.A., Gastellu-Etchegorry, J.P., and Krayenhoff, E.S. (2021). Modeling the angular effect of MODIS LST in urban areas: a case study of Toulouse, France. Remote Sens. Environ. 257, 112361. https://doi.org/10.1016/j.rse.2021.112361.

16. Zhou, D., Li, D., Sun, G., Zhang, L., Liu, Y., and Hao, L. (2015). Contrasting effects of urbanization and agriculture on surface temperature in eastern China. J. Geophys. Res. Atmos. 121, 9597–9606. https://doi.org/10.1002/2016jd025359.

17. Xiang, Y., Ye, Y., Peng, C., Teng, M., and Zhou, Z. (2022). Seasonal variations for combined effects of landscape metrics on land surface temperature (LST) and aerosol optical depth (AOD). Ecol. Indic. 138, 108810. https://doi.org/10.1016/j.ecolind.2022.108810.

18. Pinker, R.T., Ma, Y., Chen, W., Hulley, G., Borbas, E., Islam, T., Hain, C., Cawse-Nicholson, K., Hook, S., and Basara, J. (2019). Towards a unifiied and coherent land surface temperature earth system data record from geostationary satellites. Remote Sens. 11, 1399. https://doi.org/10.3390/rs11121399.

19. Weng, Q., and Fu, P. (2014). Modeling diurnal land temperature cycles over Los Angeles using downscaled GOES imagery. ISPRS J. Photogramm. Remote Sens. 97, 78–88. https://doi.org/10.1016/j.isprsjprs.2014.08.009.

20. Kogan, F., Salazar, L., and Roytman, L. (2012). Forecasting crop production using satellite–based vegetation health indices in Kansas, USA. Int. J. Remote Sens. *33*, 2798–2814. https://doi.org/10.1080/01431161.2011.621464.

21. Kogan, F.N. (2001). Operational space technology for global vegetation assessment. Bull. Amer. Meteor. Soc. *82*, 1949–1964. https://doi.org/10.1175/1520-0477(2001)082<1949:OSTFGV>2.3.CO.

22. He, B.J. (2018). Potentials of meteorological characteristics and synoptic conditions to mitigate urban heat island effects. Urban Clim. *24*, 26–33. https://doi.org/10.1016/j.uclim.2018.01.004.

23. Yin, S., Gong, Z., Gu, L., Deng, Y., and Niu, Y. (2022). Driving forces of the efficiency of forest carbon sequestration production: spatial panel data from the national forest inventory in China. J. Cleaner Prod. *330*, 129776. https://doi.org/10.1016/j.jclepro.2021.129776.

24. Qiao, Z., Liu, L., Qin, Y., Xu, X., Wang, B., and Liu, Z. (2020). The impact of urban renewal on land surface temperature changes: a case study in the main city of Guangzhou, China. Remote Sens. *12*, 794. https://doi.org/10.3390/rs12050794.

25. Deng, Y., Wang, S., Bai, X., Tian, Y., Wu, L., Xiao, J., Chen, F., and Qian, Q. (2018). Relationship among land surface temperature and LUCC, NDVI in typical karst area. Sci. Rep. *8*, 641. https://doi.org/10.1038/s41598-017-19088-x.

26. Taripanah, F., and Ranjbar, A. (2021). Quantitative analysis of spatial distribution of land surface temperature (LST). in relation Ecohydrological, terrain and socio–economic factors based on Landsat data in mountainous area. Adv. Space Res. *68*, 3622–3640. https://doi.org/10.1016/j.asr.2021.07.008.

27. Su, M.A., Ngarambe, J., Santamouris, M., and Yun, G.Y. (2021). Empirical evidence on the impact of urban overheating on building cooling and heating energy consumption. iScience *24*, 102495. https://doi.org/10.1016/j.isci.2021.102495.

28. Kong, L., Lau, K.K.–L., Yuan, C., Chen, Y., Xu, Y., Ren, C., and Ng, E. (2017). Regulation of outdoor thermal comfort by trees in Hong Kong. Sustain. Cities Soc. *31*, 12–25. https://doi.org/10.1016/j.scs.2017.01.018.

29. Yu, H., Luedeling, E., and Xu, J. (2010). Winter and spring warming result in delayed spring phenology on the Tibetan Plateau. Proc. Natl. Acad. Sci. USA *107*, 22151–22156. https://doi.org/10.1073/pnas.1012490107.

30. Zhou, D., Zhao, S., Liu, S., Zhang, L., and Zhu, C. (2014). Surface urban heat island in China's 32 major cities: spatial patterns and drivers. Remote Sens. Environ. *152*, 51–61. https://doi.org/10.1016/j.rse.2014.05.017.

31. Guha, S., Govil, H., and Besoya, M. (2020). An investigation on seasonal variability between LST and NDWI in an urban environment using Landsat satellite data. Geomat. Nat. Hazards Risk *11*, 1319–1345. https://doi.org/10.1080/19475705.2020.1789762.

32. Yang, D., Lou, Y., Zhang, P., and Jiang, L. (2022). Spillover effects of built–up land expansion under ecological security constraint at multiple spatial scales. Front. Ecol. Evol. *10*, 907691. https://doi.org/10.3389/fevo.2022.907691.

33. Yue, W., Wu, T., Liu, X., Zhang, L., Wu, C., Ye, Y., and Zhang, G. (2020). Developing an urban sprawl index for China's mega–cities. J. Geogr. Sci. *75*, 2730–2743. https://doi.org/10.11821/dlxb202012013.

34. Alexander, C. (2020). Normalised difference spectral indices and urban land cover as indicators of land surface temperature (LST). Int. J Appl. Earth Obs. *86*, 102013. https://doi.org/10.1016/j.jag.2019.102013.

35. Gogoi, P.P., Vinoj, V., Swain, D., Roberts, G., Dash, J., and Tripathy, S. (2019). Land use and land cover change effect on surface temperature over Eastern India. Sci. Rep. *9*, 8859. https://doi.org/10.1038/s41598-019-45213-z.

36. Zhou, D., Bonafoni, S., Zhang, L., and Wang, R. (2018). Remote sensing of the urban heat island effect in a highly populated urban agglomeration area in East China. Sci. Total Environ. *628–629*, 415–429. https://doi.org/10.1016/j.scitotenv.2018.02.074.

37. Xue, Z., Hou, G., Zhang, Z., Lyu, X., Jiang, M., Zou, Y., Shen, X., Wang, J., and Liu, X. (2019). Quantifying the cooling–effects of urban and peri–urban wetlands using remote sensing data: case study of cities of Northeast China. Landsc.Urban Plan. *182*, 92–100. https://doi.org/10.1016/j.landurbplan.2018.10.015.

38. Zhai, P., and Pan, X. (2003). Trends in temperature extremes during 1951-1999 in China. Geophys. Res. Lett. *30*. https://doi.org/10.1029/2003gl018004.

39. Luo, M., Lau, N., Liu, Z., Wu, S., and Wang, X. (2022). An observational investigation of spatiotemporally contiguous heatwaves in China from a 3D perspective. Geophys. Res. Lett. *49*. https://doi.org/10.1029/2022GL097714.

40. He, B.J., Ding, L., and Prasad, D. (2020). Urban ventilation and its potential for local warming mitigation: a field experiment in an open midrise gridiron precinct. Sustain Cities Soc. *55*, 102028. https://doi.org/10.1016/j.scs.2020.102028.

41. Bishal, R. (2021). Optimum machine learning algorithm selection for forecasting vegetation indices: MODIS NDVI and EVI. Remote Sens. Appl. Soc. Environ. *23*, 100582. https://doi.org/10.1016/j.rsase.2021.100582.

42. Chen, Y., Zhou, B., Zhai, P., and Moufouma-Okia, W. (2019). Half-a-degree matters for reducing and delaying global land exposure to combined daytime nighttime hot extremes. Earth's Future *7*, 953–966. https://doi.org/10.1029/2019EF001202.

43. Tippett, M.K., Lepore, C., and Cohen, J.E. (2016). More tornadoes in the most extreme U.S. tornado outbreaks. Science *354*, 1419–1423. https://doi.org/10.1126/science.aah7393.

44. Alavipanah, S., Weng, Q., Gholamnia, M., and Khandan, R. (2017). An analysis of the discrepancies between MODIS and INSAT-3D LSTs in high temperatures. Remote Sens. *9*, 347. https://doi.org/10.3390/rs9040347.

45. Goldblatt, R., Addas, A., Crull, D., Maghrabi, A., Levin, G.G., and Rubinyi, S. (2021). Remotely sensed derived land surface temperature (LST) as a proxy for air temperature and thermal comfort at a small geographical scale. Land *10*, 410. https://doi.org/10.3390/land10040410.

46. Yang, J., Wang, Y., Xiao, X., Jin, C., Xia, J.C., and Li, X. (2019). Spatial differentiation of urban wind and thermal environment in different grid sizes. Urban Clim. *28*, 100458. https://doi.org/10.1016/j.uclim.2019.100458.

47. Hao, Z. (2022). Compound events and associated impacts in China. iScience *25*, 104689. https://doi.org/10.1016/j.isci.2022.104689.

48. Jendritzky, G., de Dear, R., and Havenith, G. (2012). UTCI—why another thermal index? Int. J. Biometeorol. *56*, 421–428. https://doi.org/10.1007/s00484-011-0513-7.

49. Unal Cilek, M., and Cilek, A. (2021). Analyses of land surface temperature (LST). variability among local climate zones (LCZs) comparing Landsat–8 and ENVI–met model data. Sustain. Cities Soc. *69*, 102877. https://doi.org/10.1016/j.scs.2021.102877.

50. Ren, J., Yang, J., Zhang, Y., Xiao, X., Xia, J.C., Li, X., and Wang, S. (2022). Exploring thermal comfort of urban buildings based on local climate zones. J Clean Prod. *340*, 130744. https://doi.org/10.1016/j.jclepro.2022.130744.

51. Hrisko, J., Ramamurthy, P., Yu, Y., Yu, P., and Melecio-Vázquez, D. (2020). Urban air temperature model using GOES–16 LST and a diurnal regressive neural network algorithm. Remote Sens. Environ. *237*, 111495. https://doi.org/10.1016/j.rse.2019.111495.

52. Li, F., Zhang, X., Kondragunta, S., Schmidt, C.C., and Holmes, C.D. (2020). A preliminary evaluation of GOES–16 active fifire product using Landsat–8 and VIIRS active fifire data, and ground–based prescribed fifire records. Remote Sens Environ. *237*, 111600. https://doi.org/10.1016/j.rse.2019.111600.

53. Guo, A., Yang, J., Xiao, X., Xia Cecilia, J., Jin, C., and Li, X. (2020). Influences of urban spatial form on urban heat island effects at the community level in China. Sustain Cities Soc. *53*, 101972. https://doi.org/10.1016/j.scs.2019.101972.

54. Shi, Z., Yang, J., Zhang, Y., Xiao, X., and Xia, J.C. (2022). Urban ventilation corridors and spatiotemporal divergence patterns of urban heat island intensity: a local climate zone perspective. Environ. Sci. Pollut. Res. Int. *29*, 74394–74406. https://doi.org/10.1007/s11356-022-21037-9.

55. Yue, W., Liu, Y., Fan, P., Ye, X., and Wu, C. (2012). Assessing spatial pattern of urban

thermal environment in Shanghai, China. Stoch. Environ. Res. Risk Assess. *26*, 899–911. https://doi.org/10.1007/s00477-012-0683-1.

56. Kafy, A.-A., Islam, M., Sikdar, S., Ashrafi, T.J., Al–Faisal, A., Islam, M.A., Rakib, A.A., Khan, M.H.H., Sarker, M.H.S., and Ali, M.Y. (2021). Remote sensing–based approach to identify the influence of land use/land cover change on the urban thermal environment: a case study in Chattogram City, Bangladesh. In Re–Envisioning Remote Sensing Applications (CRC Press).

57. Yang, X., Chen, W., Jiang, M., Jiang, P., and Shen, X. (2022). Dual effects of technology change: how does water technological progress affect China's water consumption? iScience *25*, 104629. https://doi.org/10.1016/j.isci.2022.104629.

58. Yang, J., Xin, J., Zhang, Y., Xiao, X., and Xia, J.C. (2022). Contributions of sea–land breeze and local climate zones to daytime and nighttime heat island intensity. npj Urban Sustain. *2*, 12. https://doi.org/10.1038/s42949–022–00055–z.

59. FENG Yueyi, 冯., HU Tangao, 胡., and ZHANG Lixiao, 张. (2014). Impacts of structure characteristics on the thermal environment effect of city parks. Acta Eco. Sin. *34*, 3179–3187. https://doi.org/10.5846/stxb201306101641.

60. Tran, D.X., Pla, F., Latorre-Carmona, P., Myint, S.W., Caetano, M., and Kieu, H.V. (2017). Characterizing the relationship between land use land cover change and land surface temperature. ISPRS J. Photogramm. Remote Sens. *124*, 119–132. https://doi.org/10.1016/j.isprsjprs.2017.01.001.

61. Liu, F., Zhang, X., Murayama, Y., and Morimoto, T. (2020). Impacts of land cover/use on the urban thermal environment: a comparative study of 10 megacities in China. Remote Sens. *12*, 307. https://doi.org/10.3390/rs12020307.

62. Feizizadeh, B., and Blaschke, T. (2013). Examining urban heat island relations to land use and air pollution: multiple endmember spectral mixture analysis for thermal remote sensing. IEEE J. Sel. Top. Appl. Earth Obs. Remote Sens. *6*, 1749–1756. https://doi.org/10.1109/JSTARS.2013.2263425.

63. Reich, P.B., Bermudez, R., Montgomery, R.A., Rich, R.L., Rice, K.E., Hobbie, S.E., and Stefanski, A. (2022). Even modest climate change may lead to major transitions in boreal forests. Nature *608*, 540–545. https://doi.org/10.1038/s41586-022-05076-3.

64. Peng, S.S., Piao, S., Zeng, Z., Ciais, P., Zhou, L., Li, L.Z.X., Myneni, R.B., Yin, Y., and Zeng, H. (2014). Afforestation in China cools local land surface temperature. Proc. Natl. Acad. Sci. USA *111*, 2915–2919. https://doi.org/10.1073/pnas.1315126111.

65. Chen, M., Gong, Y., Lu, D., and Ye, C. (2019). Build a people–oriented urbanization: China's new–type urbanization dream and Anhui model. Land Use Pol. *80*, 1–9. https://doi.org/10.1016/j.landusepol.2018.09.031.

66. Chu, Y.W. (2020). China's new urbanization plan: progress and structural constraints. Cities *103*, 102736. https://doi.org/10.1016/j.cities.2020.102736.

67. Manoli, G., Fatichi, S., Schläpfer, M., Yu, K., Crowther, T.W., Meili, N., Burlando, P., Katul, G.G., and Bou-Zeid, E. (2019). Magnitude of urban heat islands largely explained by climate and population. Nature *573*, 55–60. https://doi.org/10.1038/s41586-019-1512-9.

68. Liang, W., and Yang, M. (2019). Urbanization, economic growth and environmental pollution: evidence from China. Sustain. Comput-Infor. *21*, 1–9. https://doi.org/10.1016/j.suscom.2018.11.007.

69. Emerson, C.W., Lam, N.S., and Quattrochi, D.A. (2005). A comparison of local variance, fractal dimension, and Moran's I as aids to multispectral image classification. Int. J. Remote Sens. *26*, 1575–1588. https://doi.org/10.1080/01431160512331326765.

70. Tillé, Y., Dickson, M.M., Espa, G., and Giuliani, D. (2018). Measuring the spatial balance of a sample: a new measure based on Moran's I index. Spat. Stat. *23*, 182–192. https://doi.org/10.1016/j.spasta.2018.02.001.

STAR★METHODS

KEY RESOURCES TABLE

REAGENT or RESOURCE	SOURCE	IDENTIFIER
Other		
GEO 10–day LST TCI https://land.copernicus.eu/global/products/lst	The 10–day TCI is calculated based on the 10–day LST product: $$\text{TCI} = \frac{[LST_{Max}]_{Max} - LST_{10DayMax}}{[LST_{Max}]_{Max} - [LST_{Max}]_{Min}}$$ $LST_{10DayMax}$ is the median LST at noon sun height over a 10–day period, $[LST_{Max}]_{Max}$ and $[LST_{Max}]_{Min}$ are the extreme value of the maximum LST per pixel at local noon.	N/A
Globe Land 30 Ministry of Natural Resources of the People's Republic of China	Coordinate system: WGS–84 Resolution: 30 m Accuracy: 85.72% A total of 53 Chinese regional images are selected and used after image fusion and sampling.	N/A
Meteorological data	Source: rp5.ru	N/A
Boundary datasets	Source: https://www.resdc.cn/	N/A

RESOURCE AVAILABILITY

Lead contact

Further information and requests for resources should be directed to and will be fulfilled by the lead contact, Jun Yang (yangjun8@mail.neu.edu.cn).

Materials availability

This study did not generate new unique materials.

Data and code availability

Any additional information required to reanalyze the data reported in this paper is available from the lead contact upon request.

METHOD DETAILS

Data

The diurnal cycle characteristics of LST can help in understanding the comprehensive change in the thermal environment and its potential mechanism, which is of great value for urban planning and assessment of urban thermal risk and vulnerability. The TCI data used in this study are calculated from the LST of the geostationary satellite, as shown in key resources table. LULC data contains 10 first–level class types (10–cultivated land, 20–forest, 30–grass land, 40–shrubland, 50–wetland, 60–water body, 70–tundra, 80–artificial surfaces, 90–bare land, and 100–permanent snow and ice). The LULC in the study area was extracted using the vector boundary. Simultaneously, the land use patterns of the second class were combined into the first class, and the land use types in Northwest, North, and South China were summarized and analyzed.

Moran's I calculation

The urban climate has cross–regional mobility, and the thermal environment of a certain area affects the surrounding area. In this study, spatial autocorrelation statistics were used to explore the correlation between the thermal environment and different spatial locations. The global Moran's I index can reflect the autocorrelation mode of the thermal environment in the entire research area, and the local Moran's I index can be used to obtain the correlation degree of each spatial unit and its neighboring units.[69,70]

The global Moran's I exponent was calculated as follows:

$$\text{Moran's } I = \frac{\sum\limits_{i=1}^{n} \sum\limits_{j=1}^{n} w_{ij}(x_i - \bar{x})(x_j - \bar{x})}{S^2 \sum\limits_{i=1}^{n} \sum\limits_{j=1}^{n} w_{ij}} \qquad \text{(Equation 1)}$$

Standardized index:

$$Z_a = \frac{I - E(I)}{\sqrt{\text{VAR}(I)}} \qquad \text{(Equation 2)}$$

The local Moran's I exponent was calculated as follows:

$$I_i = \frac{(x_i - \bar{x})}{S^2} \sum\limits_{j} w_{ij}(x_j - \bar{x}) \qquad \text{(Equation 3)}$$

$$S^2 = \frac{1}{n} \sum\limits_{i=1}^{n} (x_i - \bar{x})^2 \qquad \text{(Equation 4)}$$

$$\bar{x} = \frac{1}{n} \sum\limits_{i=1}^{n} x_i \qquad \text{(Equation 5)}$$

The Moran's I index ranged from −1 to 1. When Moran's I > 0, it indicates that the data presents a spatial positive correlation, and the larger the value, the more obvious the spatial correlation. When Moran's I < 0, it means that the data present a negative spatial correlation, and the smaller the value, the greater the spatial difference. When the Moran's I was 0, the space was randomly distributed.

Simultaneously, the P-value and Z scores should be combined to determine the degree of spatial correlation. The P-value represents the probability. When P is very small, the spatial pattern of the factor is unlikely to be generated by a random process. The Z-score represents the standard deviation multiple and can reflect the degree of dispersion of a dataset. If $p < 0.01$ and $Z > 2.58$, it indicates that the data have 99% confidence in the agglomeration distribution. If $p < 0.01$ and $Z < -2.58$, it is 99% certain that the distribution is discrete.

Statistical analysis

In this study, the response modes of LULC and TCI were explored in two ways: city and grid modes. First, the spatial and temporal distribution of TCI and LULC raster data at the urban scale was obtained using the urban vector boundary. Second, the Create Fishnet tool of ArcGIS 10.7 was used to create a 5 × 5 km grid as a spatial range, and the TCI value distribution of LULC under the faceted grid were explored through statistical analysis to ensure the reliability of the study.